Accepted Manuscript

Determination of strength and debonding energy of a glass-concrete interface for encapsulation-based self-healing concrete

F.A. Gilabert, K. Van Tittelboom, E. Tsangouri, D. Van Hemelrijck, N. De Belie, W. Van Paepegem

PII: S0958-9465(17)30093-8

DOI: 10.1016/j.cemconcomp.2017.01.011

Reference: CECO 2770

To appear in: *Cement and Concrete Composites*

Received Date: 12 April 2016

Revised Date: 16 December 2016

Accepted Date: 19 January 2017

Please cite this article as: F.A. Gilabert, K. Van Tittelboom, E. Tsangouri, D. Van Hemelrijck, N. De Belie, W. Van Paepegem, Determination of strength and debonding energy of a glass-concrete interface for encapsulation-based self-healing concrete, *Cement and Concrete Composites* (2017), doi: 10.1016/j.cemconcomp.2017.01.011.

Determination of strength and debonding energy of a glass-concrete interface for encapsulation-based self-healing concrete

F. A. Gilabert[a,d,*], K. Van Tittelboom[b], E. Tsangouri[c,d], D. Van Hemelrijck[c], N. De Belie[b], W. Van Paepegem[a]

[a] *Ghent University, Department of Materials Science and Engineering, Faculty of Engineering and Architecture, Tech Lane Ghent Science Park - Campus A, Technologiepark-Zwijnaarde 903, 9052 Zwijnaarde (Ghent), Belgium.*
[b] *Ghent University, Department of Structural Engineering, Magnel Laboratory for Concrete Research, Faculty of Engineering and Architecture, Tech Lane Ghent Science Park - Campus A, Technologiepark-Zwijnaarde 904, 9052 Zwijnaarde (Ghent), Belgium.*
[c] *Vrije Universiteit Brussel, Department of Mechanics of Materials and Constructions, Faculty of Engineering, Pleinlaan 2, 1050 Brussels, Belgium*
[d] *SIM vzw, Technologiepark-Zwijnaarde 935, 9052 Zwijnaarde (Ghent), Belgium.*

Abstract

This paper presents a combined experimental-numerical analysis to assess the strength and fracture toughness of a glass-concrete interface. This interface is present in encapsulation-based self-healing concrete. There is absence of published results of these two properties, despite their important role in the correct working of this self-healing strategy. Two setups are used: uniaxial tensile tests to assess the bonding strength and four point bending tests to get the interfacial energy. The complementary numerical models for each setup are conducted using the finite element method. Two approaches are used: cohesive zone model to study the interface strength and the virtual crack closure technique to analyze the interfacial toughness. The models are validated and used to verify the experimental interpretations. It is found that a glass-concrete interface can develop a maximum strength of approximately 1 N/mm^2 with fracture energy of 0.011 J/m^2.

Keywords: self-healing concrete, material interfaces, debonding, cohesive zone model, virtual crack closure technique, finite element method

1. Introduction

The general strategy of encapsulation-based self-healing materials relies on inserting small fluid-filled capsules in a matrix. [1–10]. The working principle of this autonomic healing strategy depends upon an adequate release of the capsule content whenever the matrix is internally damaged. When the capsules are intercepted by cracks of the matrix, the stress at the crack tip is transferred to the capsule. This stress should trigger the capsule breakage and, thus the internal fluid could spread into the crack space via capillarity. To complete the healing process, this fluid is capable of curing after some reaction, in such a way that the crack path is sealed and the final internal structure is partially repaired [11].

When this encapsulation-based self-healing strategy is applied to concrete structures, capsules made of glass are often used [12–15]. This choice is mainly due to the brittleness matching of both materials at the scale size of the concrete constituents. However, embedding a glass capsule in a concrete matrix always creates an interface between both elements. If this interface is not able to bear the load transfer, an incoming crack will simply trigger a premature debonding, similarly to what happens when a solid inclusion is weakly bonded to a matrix [16, 17]. As a consequence, although the debonding would create a hole-liked region where the crack would be attracted, the crack would simply pass along the capsule perimeter and continue its path again through the matrix [18–20]. This situation would result in an intact capsule and thus the process of healing would not occur as expected. As mentioned, this encapsulation-based strategy relies on the fact that the capsules should break immediately after they are intercepted by a crack, however this is not always the case. This is a phenomenon that can be hardly inferred from the overall mechanical response of the test. In fact, once the experimental test is finished, it is

*Corresponding author. Tel.: +32 9 331 04 09.
Email address: fran.gilabert@ugent.be (F. A. Gilabert)

often very difficult to know if the capsules broke at the right moment just after the crack arrival, and not some time later, after the crack has already propagated causing an excessive deformation which is difficult to repair. To the author's best knowledge, this situation is not treated in the literature and deserve further analysis. The mechanical properties of this interface have received less attention, and its properties have not been the main object of mechanical characterization. However, the current interest in this self-healing strategy is leading to an increase of theoretical and numerical works with the aim of getting a better understanding of its mechanisms and determining the key factors to improve efficiency and feasibility [8, 21–27]. These models assume either perfect bonding or a certain range of typical values of the interface properties, which are selected as a function of mechanical similarities given by composition or the degree of brittleness [28, 29]. Further assessment and discussion of how this glass-concrete interface affects the self-healing efficiency lies out of the scope of the present paper, and it will be treated in forthcoming publication.

The motivation of this work is twofold: first, to quantify the strength and brittleness of this type of interface, whose values have been unknown so far, and second, to provide a consistent and robust combined experimental-modeling procedure to get these values. Two fundamental properties of the glass-concrete interface are characterized: its maximum tensile strength and its fracture toughness. Maximum tensile strength, hereafter referred to as bonding strength, provides a measure of the static normal load required to separate a piece of concrete fully adhered to a flat glass surface. This bonding strength corresponds to the mode I of fracture. This measure is a material property (or interface property), which is independent of the geometrical features of the interface (maximum allowable interfacial tensile stress). Effectively, in a real situation with cylindrical capsules subjected to a multiaxial load, not only mode-I would occur, but mode-II (in-plane shear) or mode-III (out-of-plane shear) might be also present. Nevertheless, from pull-out tests using borosilicate glass capsules embedded in the same type of concrete, the shear strength values are in the same order of magnitude. This shear mode was previously assessed by Van Tittelboom [30] and its value was determined from direct pull-out testing of a glass capsule embedded in a mortar and concrete cylinders. However, this test is extremely delicate and it presents many difficulties related to the clamping and the alignment of the capsule, among others. This situation leads to a quite large data dispersion. On the other hand, fracture toughness provides a measure of the difficulty to extend an existing interfacial crack between the two aforementioned adhered surfaces. The four-point-bending test makes it possible to determine the total interface energy using a simple flat geometry, where both modes-I and II are cooperating. This is an intrinsic property of the interface that depends on the interface nature, but not on the geometric features. A similar treatment could have been performed using a curved composed beam, although from the mathematical point of view, the derivation of an analytical formula for the total fracture energy would have been much more tedious to obtain. For the sake of simplicity and as a first approach, during the analysis of the propagation of the interfacial crack, this work considers an isotropic behavior, and therefore, the energies related to mode I and mode II are equal.

Regarding the applicability of the results from the proposed methodology, several aspects of the fracture process of capsules in self-healing based materials can be afforded from the simulation point of view. As an example, the analysis of the effect of the capsule shape (e.g., spherical, tubular) and size (length, diameter, thickness) on the capability of its debonding or fracture within the matrix can be carried out. The properties obtained from the present paper can be directly used to feed traction-separation laws using cohesive elements in finite element models [25, 27, 31, 32]. From the practical point of view, if the capsule-matrix interface strength has to be increased but the capsules surfaces cannot be previously treated with additives, its geometrical features could be chosen in such a way that it triggers the capsule breakage more easily under certain types of stress fields. This type of analyzes are very suitable for numerical simulations, where the ratio between the capsule strength to the bonding interface also has to be taken into account as a function of the capsule dimensions.

This work is organized as follows. Two blocks are well distinguished: section 2 is entirely devoted to the experimental part, whereas section 3 deals with the numerical modeling. Within the experimental part, three sections have been differentiated: section 2.1 presents the complete process to produce the concrete material as well as its mechanical characterization, section 2.2 describes the experimental setup required to determine the interfacial bonding strength and section 2.3 deals with the setup to assess the interfacial fracture toughness. Likewise, these two last sections share the same structure: firstly, the design and the sequence performed to prepare the specimens are described, second, the details of the mechanical setup and the instrumentation to

Constituent	Amount (kg/m^3)
Sand 0/4	670
Gravel 2/8	490
Gravel 8/16	790
CEM I 52.5 N	300
Water	150

Table 1: Concrete composition.

carry out the measurements are shown, and finally, the obtained results are presented and briefly discussed. In a similar fashion, the numerical part exposed in section 3 is composed of two sections dedicated to the two numerical setups, namely section 3.1 treats the simulation model used to analyze the tensile bonding strength and section 3.2 deals with the four point bending model to investigate the interfacial toughness. Within the section for each model, a description of the interface modeling technique is provided, as well as complete details about the adopted numerical approaches (axi-symmetry, 2D, 3D, boundary conditions, type of mesh and element). In that sense, the reliability and accuracy for each model are thoroughly studied regarding the type and size of the mesh. Finally, the results obtained from the models are compared to the experiments and some additional insights provided by the simulations are also discussed regarding the experimental observations. This work finishes providing a summary of the findings and with some remarks about the applicability of the results.

2. Experimental

2.1. Concrete characterization

The concrete characteristics, presented in this section, have been used as input to prepare the test samples described in sections 2.2 and 2.3. In addition, the elastic properties of the concrete have been used as input data for the simulation models developed to complement the experimental procedures to assess the glass-concrete interface properties.

2.1.1. Composition

Concrete samples were prepared using the concrete composition shown in Table 1. The slump, air content and density of the fresh concrete mixture were measured on the first batch which was prepared and amounted to 15 mm, 1.9% and 2400 kg/m^3, respectively. Samples were demolded one day after casting and subsequently stored under water at a temperature of 20°C until they were 21 days old. Afterward, samples were stored in standard laboratory climate at 20°C until the time of testing at the age of 28 days.

2.1.2. Elastic properties

For each concrete batch, the compressive strength was determined at the age of 28 days on three concrete cubes with dimensions of 150 mm x 150 mm x 150 mm, according to the standard NBN EN 12390-3. Before the start of this destructive test procedure, the density of the hardened concrete was determined on each of these cubes using the sample dimensions and mass. The mean compressive strength and density amounted to 57 N/mm^2 and 2395 kg/m^3, respectively, as reported in Table 2.

The concrete tensile strength was measured on cylinders with a diameter of 50 mm and a height of 150 mm which were drilled from 150 mm x 150 mm x 600 mm prisms. At the age of 28 days, uniaxial tensile tests were performed onto five concrete cylinders and resulted in a mean value of the tensile strength of 3.1 N/mm^2 (Table 2). In order to determine the Young's modulus and the Poisson coefficient of the concrete, three cylinders with a diameter of 150 mm and a height of 300 mm were prepared. On each cylinder, three 120 mm long strain gauges were attached in axial direction, at positions equally divided along the mantle surface (see Fig. 1). The middle of each strain gauge was positioned at half height of the cylinders. Three more, identical, strain gauges were attached to each cylinder in transverse direction. These were also positioned at half height of the cylinder and covered altogether almost the complete periphery (see Fig. 1). All strain gauges were attached to the concrete surface by means of methyl methacrylate based glue.

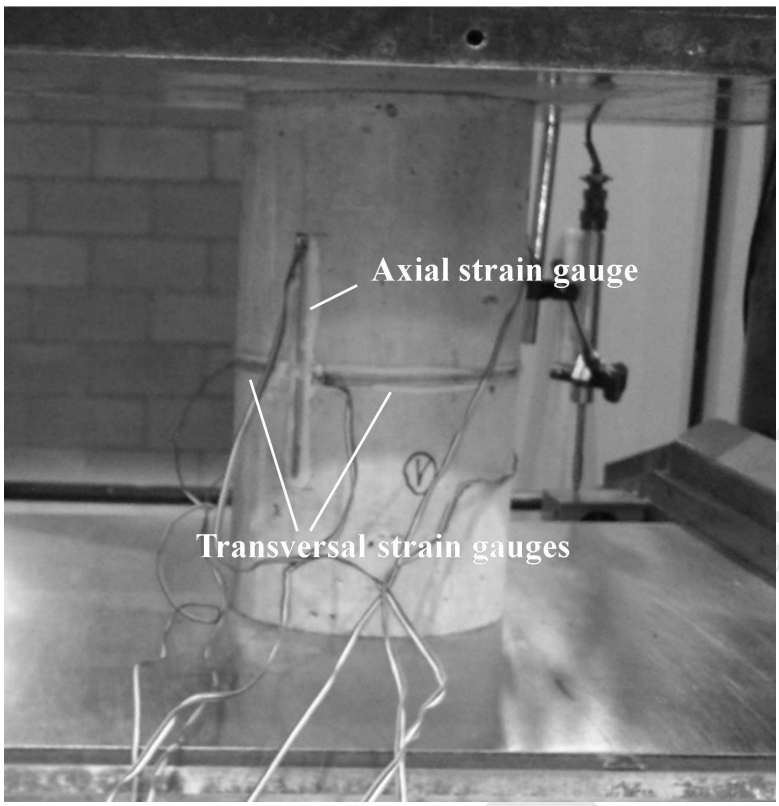

Figure 1: Setup used to determine the Young's modulus and the Poisson coefficient.

Determination of the Young's modulus (E_c) was done according to the specifications given in the standard NBN B 15-203. In short, at the age of 28 days, each cylinder was mounted in a compression test machine. Each cylinder was loaded in a cyclic compression test as shown in Fig. 2. The load cycle consisted of the following steps: load increase until 1/3 of the sample's compressive strength (σ_a) (value estimated based on the compressive strength determined on the concrete cubes), load maintained for 90 seconds, unloading at a speed of 0.6 kN/s until the stress in the concrete amounts to 1.2 N/mm^2 (σ_b), load kept constant for 90 seconds. This loading regime was repeated three times for each sample. As shown in Fig. 2, after the last unloading step, samples were immediately reloaded until complete failure.

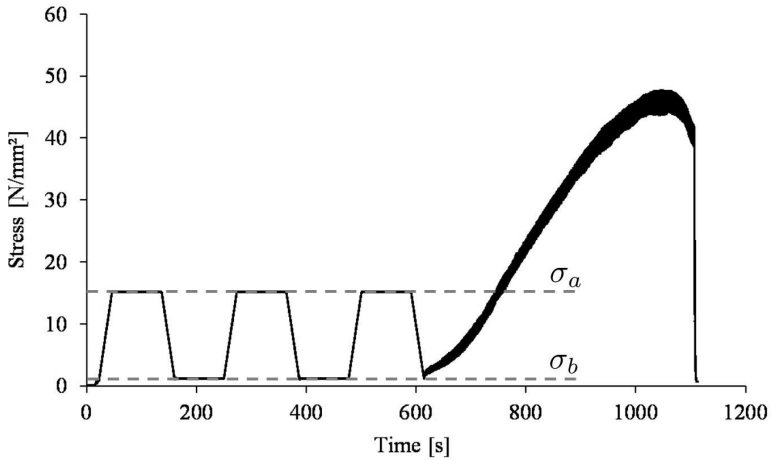

Figure 2: Cyclic loading regime used to determine the Young's modulus and the Poisson coefficient.

For the second and the third loading cycle, the strain (ϵ_0) was calculated based on the deformations measured by each axial strain gauge, according to equation 1.

$$\epsilon_0 = \frac{l_a - l_b}{L_0} \tag{1}$$

Table 2: Concrete properties (n=number of repetitions).

Property	Unit	Fresh properties Value	n
Slump	mm	15	1
Air content	%	1.9	1
Density	kg/m^3	2400	1
Property	**Unit**	**Hardened properties Value**	**n**
Density	kg/m^3	2395	6
Compressive strength	N/mm^2	57	6
Tensile strength	N/mm^2	3.1	5
Young's modulus	N/mm^2	39567	3
Poisson's ratio	–	0.17	3

where L_0 is the length of the strain gauge and l_b and l_a are the values measured by the strain gauges at σ_b and σ_a stress levels, respectively. Subsequently, the mean value for the three axial strain gauges was calculated (ϵ_m) and finally, the Young's modulus of each cylindrical sample was calculated using equation 2.

$$E_c = \frac{\sigma_a - \sigma_b}{\epsilon_m} \tag{2}$$

As shown in Table 2, a mean value of 39567 N/mm^2 was obtained for the Young's modulus of the concrete used within this study. Calculation of the Poisson coefficient (ν_c) was done using both the strain values obtained from the axial and the transversal strain gauges. For each of the three loading cycles, the mean strain obtained by the three axial and transversal strain gauges when samples were loaded at 1/3 of their compressive strength was used for the calculation. The strain obtained in transverse direction was divided by the strain obtained in axial direction to find the Poisson coefficient. These values were averaged for each loading cycle and each sample to result in the final value of 0.17 as reported in Table 2.

2.2. Bonding strength: tensile test

In this section the bond strength between glass and concrete is experimentally determined by performing a unidirectional tensile test onto a concrete cylinder casted on a circular glass plate. Since debonding between the glass and concrete matrix is the only mechanism of failure, the maximum force measured during this test can be used to calculate a characteristic value of the maximum tensile strength in a glass-concrete interface.

2.2.1. Specimen design and preparation

In order to prepare the samples, glass plates with a diameter of 100 mm and a thickness of 3.5 mm were used as the bottom of a cylindrical mold. The glass capsules used to test large-scale self-healing concrete beams are typically made of borosilicate glass [33, 34], therefore the same type of glass was chosen for the glass plates used in this work. Before use, the glass plates were degreased with acetone. Then, the molds of the samples were further built up by the use of a polyvinylchloride (PVC) tube with an internal diameter of 100 mm and a height of 53.5 mm. A saw cut was provided in the tubes in longitudinal direction to allow easy demolding of the samples. The PVC tubes were clamped around the glass plates by means of a tie strap, after which the molds were ready and casting of the concrete could start.

The concrete composition specified in section 2.1.1 was used to cast six glass-concrete cylinders as shown in Fig. 3. By analogy with the previously mentioned samples, these cylinders were demolded after one day and stored under water until the age of 21 days. Afterward they were stored in standard laboratory climate at 20°C. Within the last week of storage, cylindrical metal dollies with a diameter of 100 mm were glued with epoxy resin at both sides of the samples. Care was taken that no glue bridged the connection between the glass plate and the concrete matrix. At the age of 28 days a uniaxial tensile test was performed on the samples as described in the next section.

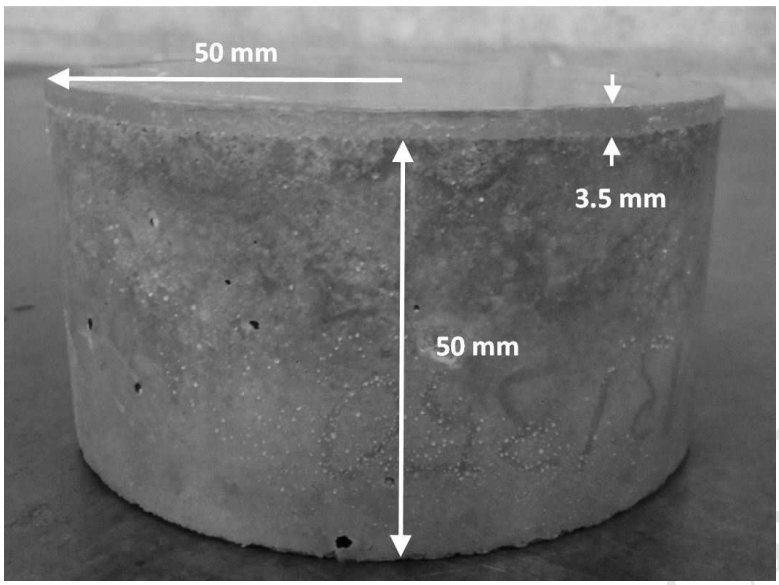

Figure 3: Glass-concrete cylinder after demolding of the sample.

2.2.2. Mechanical test setup

A first batch composed of three samples (labeled as I, II and III) was tested in a hydraulic tensile test machine with a capacity of 50 kN. Coupling devices with screw thread, which fitted inside the metal dollies, were used to connect the samples to the test machine. During testing of this first batch only the maximum force was registered for each sample. As expected, the failure process took place clearly at the glass-concrete interface, and it occurred in a very brittle way. In order to get some additional insights of the debonding process, a second

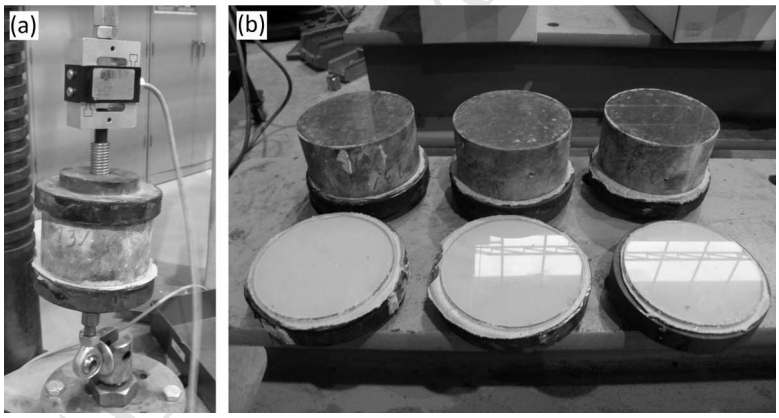

Figure 4: (a) Setup of the uniaxial tensile test. (b) Samples after loading in the uniaxial tensile test showing debonding of the glass-concrete interface.

batch of samples (labeled as IV, V and VI) were instead mounted in a servo-hydraulic tensile test machine. These samples were similarly clamped to this machine using the same coupling devices used during the first batch showed in Fig. 4a. For this second batch of samples, a load cell of 50 kN was also connected in between the sample and the machine and they were loaded in a load-controlled tensile test with a speed of 0.17 kN/s. However, in this occasion three LVDT's (Solartron AX/0.5/S) with a measurement range of ± 500 μm and an accuracy of 1 μm were attached to these samples during loading, to measure the displacement between the glass plate and the concrete in axial direction. A PVC block with a hole used to clamp the LVDT was glued at the concrete surface just above the glass-concrete interface at three positions, equally divided along the sample's circumference. At these same positions a metal hook was glued onto the lower dolly. These were used to place the tip of the LVDT.

Sample	Bond strength [N/mm^2]
I	1.15
II	0.92
III	0.70
IV	0.79
V	0.82
VI	1.36
Average	0.96±0.09

Table 3: Bond strength of a glass-concrete interface.

2.2.3. Results

Based on the maximum load measured for each sample at the moment of debonding and the sample's cross-section, the bond strength was calculated as shown in Table 3. Figure 4b shows the typical aspect of the samples after testing. All samples exhibited a very clean debonding between the glass and concrete and there were no decohesion fragments of concrete on the glass plate.

Figure 5 shows the load displacement curves obtained from the second batch composed of samples IV, V and VI. As mentioned before, the samples failed in a very brittle way and thus the measured displacement between the glass-concrete interface was really limited. For some LVDT's even negative values were obtained due to the fact that there were some imperfections in the position of the load.

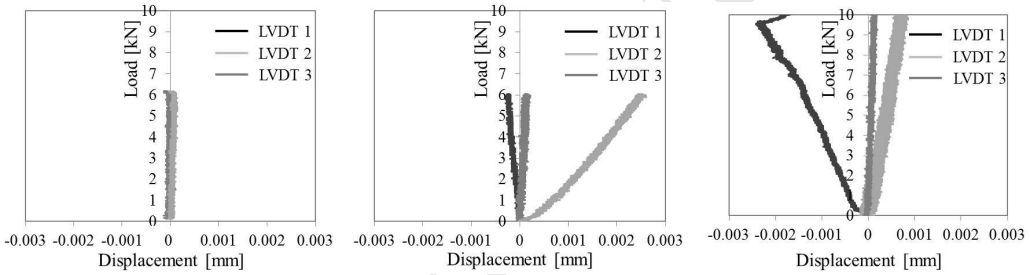

Figure 5: Load displacement diagrams obtained for samples IV, V and VI.

As it will be shown later, the simulation of this test predicts displacements which are below the accuracy of the LVTD gauges ($< 1\mu$m). Due to this reason, the reliability of the displacements registered during these tests are for guidance only. On the other hand, the force measurements are reliably accurate. In that sense, in spite of the fact that two batches were tested using two different mechanical test machines, the results have exhibited an acceptable reproducibility taking into account the typical high uncertainty inherent to cementitious materials.

2.3. Interface energy: four point bending test

The aim of this test is to obtain a characteristic energy release rate value that quantifies the degree of brittleness of a typical glass-concrete interface. This value can be used in numerical models that might contain this combination of materials. To do that, four point bending tests were performed using composed beams consisting of a lower layer of glass and an upper layer of concrete. This test setup triggers delamination of the beam and makes it possible to assess the debonding fracture toughness. The energy release rate for this configuration was obtained as demonstrated by Charalambides et al. [35]. It is important to note that the assessment of the interfacial toughness involves bending the composed beam, however, the value of the applied deflection itself is not required. As explained in ref. [35], only the value of the constant moment in which the delamination regime takes place is required, namely, the plateau in the force-displacement curve. Section 2.3.4 presents a brief description of the mathematical relationships required to link the applied force to the interfacial toughness energy.

2.3.1. Specimen design and preparation

Four composed beams were prepared and every beam consisted of two glass plates adhered to a thicker concrete beam as is schematically depicted in Fig. 6. The glass plates used for these samples were of the same

type as those used in the previous test. In order to prepare the samples, four molds (see Fig. 7a) with internal dimensions of 100 mm x 48 mm x 800 mm were used. At the bottom of these molds two glass plates with a thickness of 8 mm and a length of 399 mm were positioned so that they covered almost the complete bottom of the mold, as it is shown in Fig. 7a. These plates were first degreased with acetone. The small separation

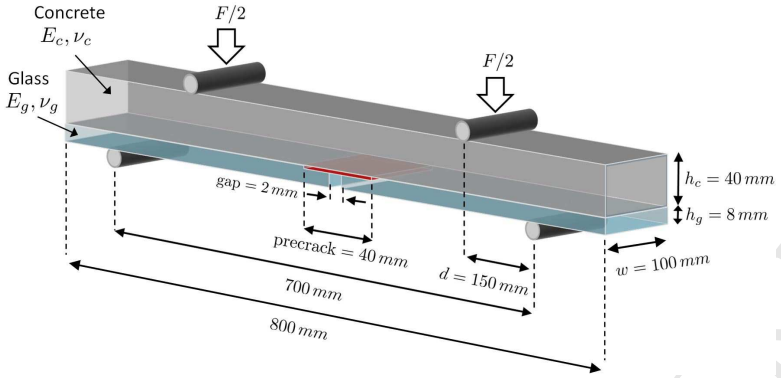

Figure 6: Dimensions of the composed beam.

of 2 mm in between both glass plates (see Fig. 7b) was filled by means of a dense foam strip which could be removed at the moment of demolding. This gap prevents any contact between the edges of the glass plates in case of debonding during testing. Introduction of a pre-crack (zone where there is no bonding between the glass

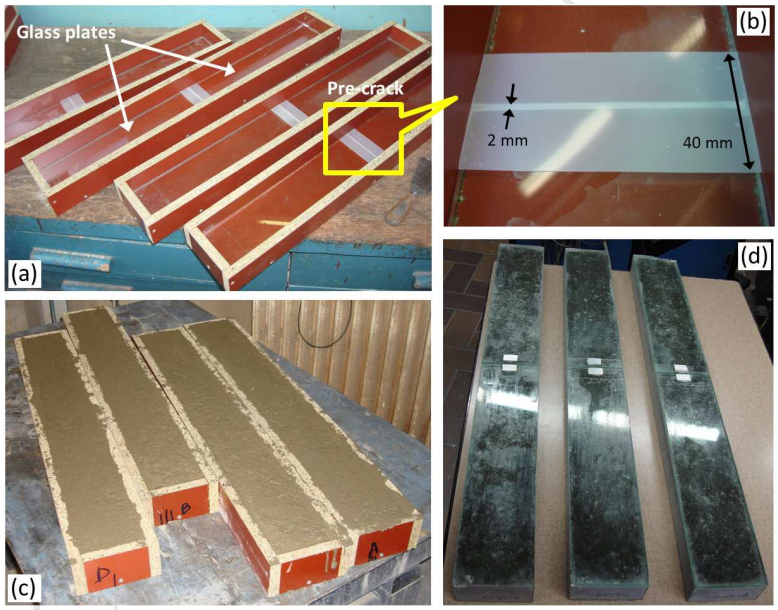

Figure 7: (a) Introduction of the glass plates in the molds. (b) Detailed view of the pre-crack preparation using a plastic spacer of 0.3 mm thickness. (c) Molds filled with fresh concrete. (d) Samples completed and ready to be tested.

and the concrete) was performed by means of a plastic spacer with a calibrated thickness of 0.3 mm, a width of 100 mm and a length of 40 mm. As Fig. 7b shows, this plastic strip was symmetrically positioned over the 2 mm gap in between both glass plates. A water film between the glass plate and the plastic strip assured that the strip remained at its position during concrete casting. The same concrete mix as described in section 2.1.1 was used here to cast four glass-concrete beams. Figure 7c shows the molds after they were filled to the top in such a way that final beams consisting of a glass layer of 8 mm and a concrete layer of 40 mm were obtained. In analogy with the other samples, demolding of the beams was performed one day later, after which the samples were stored under water until the age of 21 days. Testing in four point bending was performed at the age of 28 days. Figure 7d shows the aspect of the samples fully prepared just before the testing process (from this picture, the forth beam was already mounted in the testing machine).

2.3.2. Mechanical test setup

An Instron electro-mechanical machine (model 5885H) with a 200 kN load cell was used for loading the composite beams. The beams were mounted in the four point bending configuration shown in Fig. 8. The sample rested on an adjustable support to fit the span distance and a pivotal support ensured a uniform bending load. The machine was programmed to impose a displacement rate of 0.04 mm/min. In that sense, to guarantee a uniform contact between the anvil's rollers and the top beam surface, two steel plates were placed in between them. Fresh cement paste was used to accommodate and attach these steel plates in a way that enabled to get complete contact applying a slight load. The setup was ready one hour after the cement paste had cured. On the other hand, to prevent premature fracture of the glass plates in contact with the lower rollers, a thin polymeric band was inserted in between them.

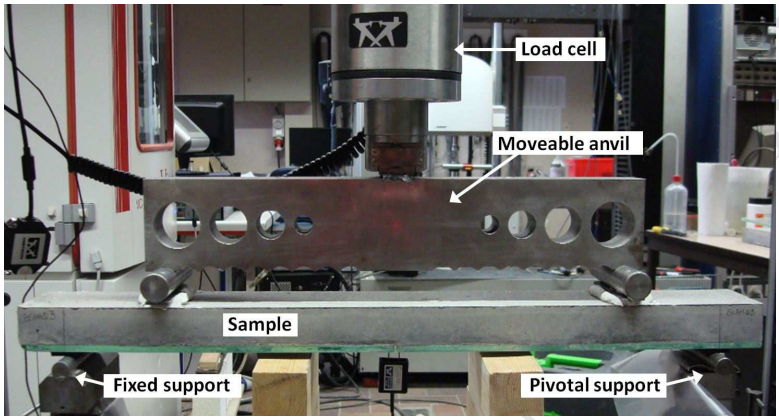

Figure 8: Four point bending setup.

2.3.3. Test results

Figure 9 shows the load displacement curves obtained from four composed beams prepared in section 2.3.1. The displacement represented in this figure corresponds to the total movement imposed to the moveable anvil (see Fig. 8). This anvil is tightly connected to the crosshead of the machine and its displacement is continuously recorded by the controller software.

These four samples have exhibited the same three-stage behavior. An initial linear dependence appears as a consequence of the bending stiffness of the sample before any debonding. This slope finishes resulting in a steady-state on the load response (see zoomed view in Fig. 9). This constant regime can be explained by the existence of an interface crack that propagates between the loading lines, as it is demonstrated by Charalambides et al. [35]. Once this plateau finishes, a new slope is generated until the breakage of the concrete beam. This last region corresponds to the bending process undergone only by the concrete layer. During the generation of this slope, the interfacial crack front stopped beneath the load line. The maximum force of this curves provides the force required to break the concrete layer. The zoomed view in Fig. 9 shows the region around the peak force produced at the beginning of the steady-state of the loading process. This peak might have several reasons, for example, as a result of nucleation of interfacial cracks in a non-precracked sample [36] or due to the formation of small cracks through the thickness that would connect the external surface of the sample with internal interfacial pre-cracks [37]. However, in the present case, this peak could be explained by the presence of some residual cement paste still existing in the 2 mm gap between glass edges (see Fig. 10a). As it is mentioned in section 2.3.1, a dense sponge strip to fill it was inserted. Although the most of this strip was removed once the concrete sample cured (this operation had to be executed very gently in order to prevent perturbation of the pre-crack), some hardened rests could still be linking both glass edges. Similarly, the two lateral joint lines formed between the glass plate and the concrete beam were also carefully cleaned, however, a gentler friction around the gap could have left some residual cement paste. Figure 10b shows the aspect of one of the samples at the end of the test, where both plates were debonded but only one side of the concrete broke.

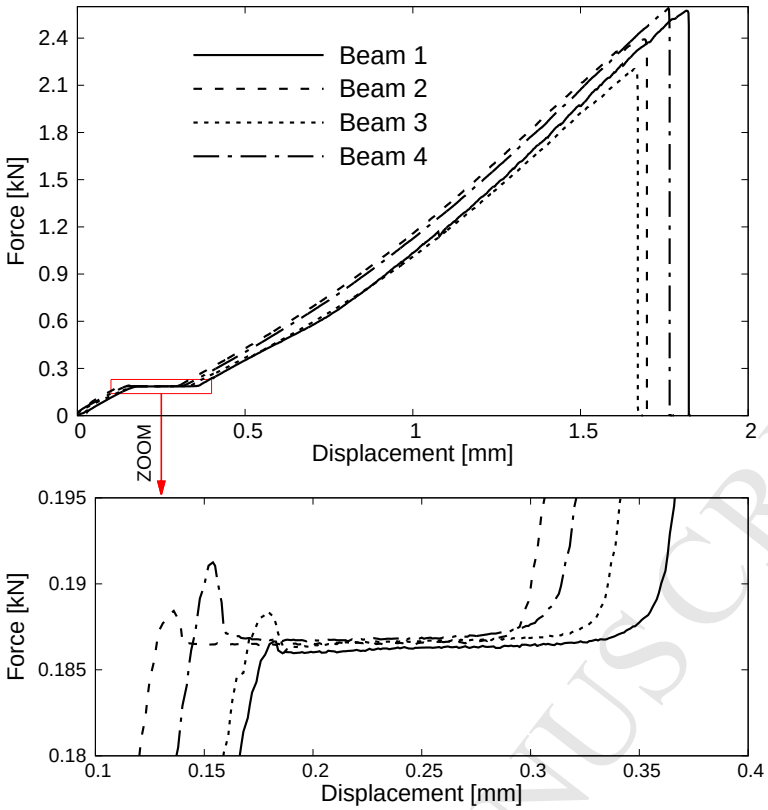

Figure 9: (Top) Force-displacement diagrams obtained from the four point bending setup. (Bottom) Zoomed view of the load region that corresponds with delamination of glass plates.

2.3.4. Calculation of the interface fracture toughness

The interfacial precrack of the bimaterial beam shown in Fig.10a is subjected to a mixed mode loading in a four point bending test. Mixed-mode conditions are quantified by a mode-mixity phase angle, which is $0°$ for pure mode-I and $90°$ for pure mode-II. This test geometry produces mixed mode loading with an angle phase of $\sim 45°$ [35, 36, 38–41]. As it is shown by Charalambides et al. [35], to obtain the individual stress intensity factors (K_I and K_{II}) an extra analysis is required. However, a quantitative distinction between both stress intensity factors lies out of the scope of this work, and therefore only the glass-concrete interfacial toughness is dealt with. Whilst the interfacial crack tip has not reached the region beneath the loading line, the portion of the composed beam between both loading lines is subjected to a constant moment. Therefore, an expression for the steady-state interfacial fracture energy can be obtained assuming that the material is linear elastic [35] given by

$$G^* = \frac{1-\nu_c^2}{8E_c}\left(\frac{Fd}{w}\right)^2\left(\frac{1}{I_c}-\frac{\lambda}{I^*}\right) \tag{3}$$

where F is the applied load, w is the sample width, d stands for the distance between the lower support and the line of load (see Fig.6), E is the Young's modulus, ν is the Poisson's ratio and the subscript "c" stands for concrete. Regarding I_c and I^*, they are the second moment of area of the concrete layer and the composed beam, respectively, both given by

$$\begin{aligned} I_c &= \frac{h_c^3}{12} \\ I^* &= \frac{h_g^3}{12} + \lambda\frac{h_c^3}{12} + \frac{\lambda h_g h_c (h_g+h_c)^2}{4(h_g+\lambda h_c)} \end{aligned} \tag{4}$$

where h is the thickness, the subscript "g" stands for glass and λ is the elastic ratio given by

$$\lambda = \frac{E_c(1-\nu_g^2)}{E_g(1-\nu_c^2)}. \tag{5}$$

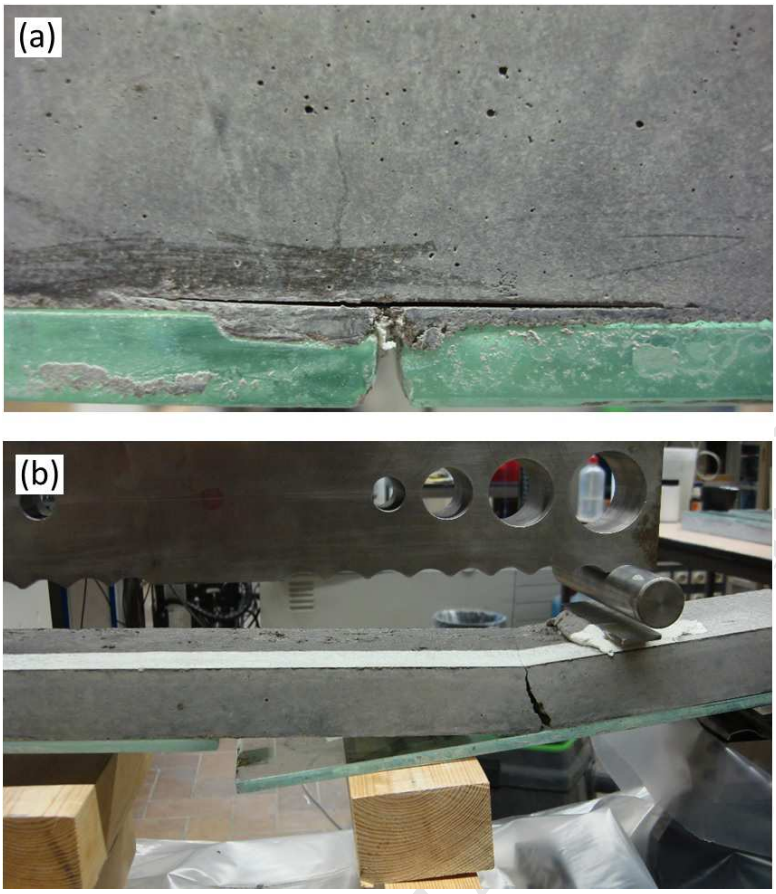

Figure 10: (a) Detailed view of the pre-crack during the initial stage of the loading process. (b) Test finalized when the concrete beam breaks.

Sample	Plateau force [N]	G^* [mJ/m^2]
Beam 1	185.23	10.57
Beam 2	186.39	10.59
Beam 3	185.65	10.62
Beam 4	186.37	10.70
Average	185.9±0.2	10.62±0.02

Table 4: Bending force and critical energy release rate of a glass-concrete interface obtained via four point bending setup.

Table 4 summarizes the results obtained from the glass-concrete debonding stages. The force values corresponding to the plateau of every curve shown in Fig. 9 were calculated by means of linear fitting to a horizontal segment. The length of every curve segment was determined detecting curvature changes. Then, energy release rate G^* corresponding to this critical load was calculated using the expressions 3, 4 and 5. The experimental value of the interface toughness obtained was approximately 0.011 J/m^2, which confirms the highly brittle nature of this type of interface.

3. Finite element modeling

3.1. Simulation of the tensile test setup

According to the experimental setup presented in section 2.2, two simulation models using different approaches have been performed: a three-dimensional model (3D) and an axisymmetric model (Axi). The aim of these models is twofold. First, these models are used to verify the correspondence between the experimental force obtained from the tensile test and the bonding strength provided as input data in the traction-separation law implemented via cohesive surfaces. Secondly, using two different approaches (namely, 3D and Axi) makes it possible to analyze which model produces more reliable results.

Table 5: Material properties: E - Young's modulus, ν - Poisson's ratio, σ^* - maximum interface tensile strength and G^* - interface fracture toughness.

Region	Material property	Value
Concrete block	E_c (N/mm^2)	39567
	ν_c (-)	0.17
Glass plate	E_g (N/mm^2)	70000
	ν_g (-)	0.21
Glass-concrete interface	σ^* (N/mm^2)	0.923
	G^* (J/m^2)	0.011

3.1.1. Geometry, boundary conditions, materials and interface

Figure 11 shows a schematic view with the geometrical details and the regions that compose the model. The specimen geometry consists of a cylindrical concrete block of height h_c and radius R attached to a cylindrical glass plate of thickness h_g and equal radius. The 3D model has been implemented as a quarter geometry of the real problem, where planes XY and YZ are symmetry planes. The Axi model corresponds with the geometry in the plane XY, where the y-axis is the axis of revolution.

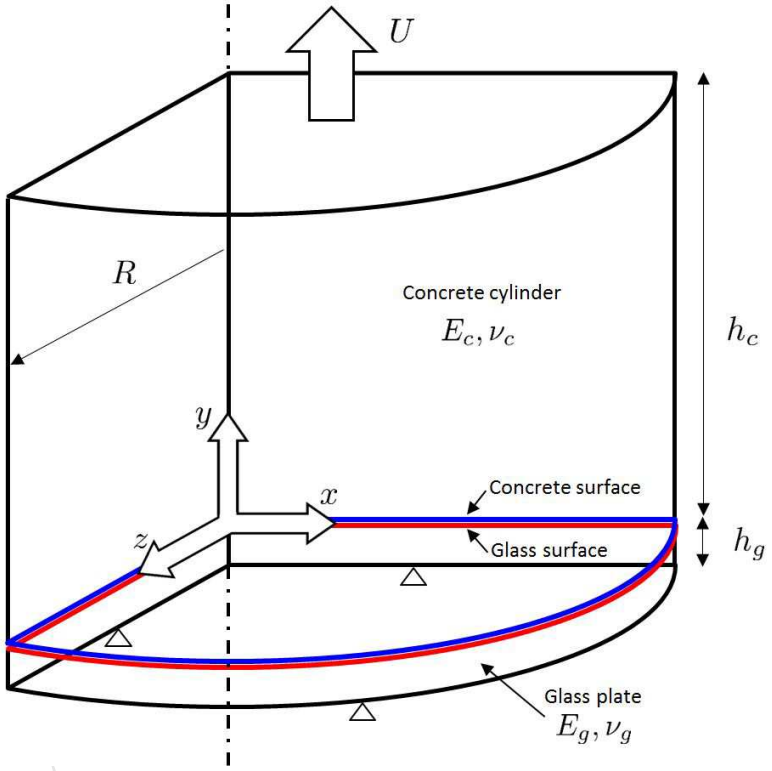

Figure 11: Model setup: geometric parameters, global system of reference, boundary conditions and detail of the surface regions affected by the cohesive law.

Regarding the boundary conditions, similarly to the experimental setup, the bottom surface of the glass plate is clamped to the machine and therefore its vertical movement is not allowed. The circular sides of the concrete and glass plate are free-faces (or free-edges in the Axi model). The top face of the concrete cylinder undergoes a uniform displacement parallel to the y-axis constantly increased as a linear function of time, so that $U = (U_{max}/T) \cdot t$, with $t \in [0, T]$. In all simulations the value $T = 1$ has been set. As it has been observed from the experimental results, the bonding interface has exhibited an extremely brittle behavior and therefore a very low displacement has to be imposed. For all simulations presented in this section a total displacement given by $U_{max} = 0.004$ mm has been used.

According to the experimental values of the material properties presented in previous section 2, Table 5 summarizes the values used in the models (3D and Axi). The value chosen for the maximum interface strength,

σ^*, equals the value of sample II (these simulations were carried out before completing the tensile tests on the second batch of samples). For the values of the concrete elastic properties and the interfacial fracture toughness, average values of previous experimental tests have been used. Concerning the elastic properties of the glass plates, values from the literature have been chosen [42].

In order to include the bonding between the concrete and the glass plate, two surface regions depicted in Fig. 11 are distinguished: the bottom surface of the concrete block (blue) and the top surface of the glass plate (red). The interaction that connects both surfaces has been implemented through a surface-based cohesive behavior that follows the traction-separation law of Fig. 12. This traction-separation law is built using a bi-linear

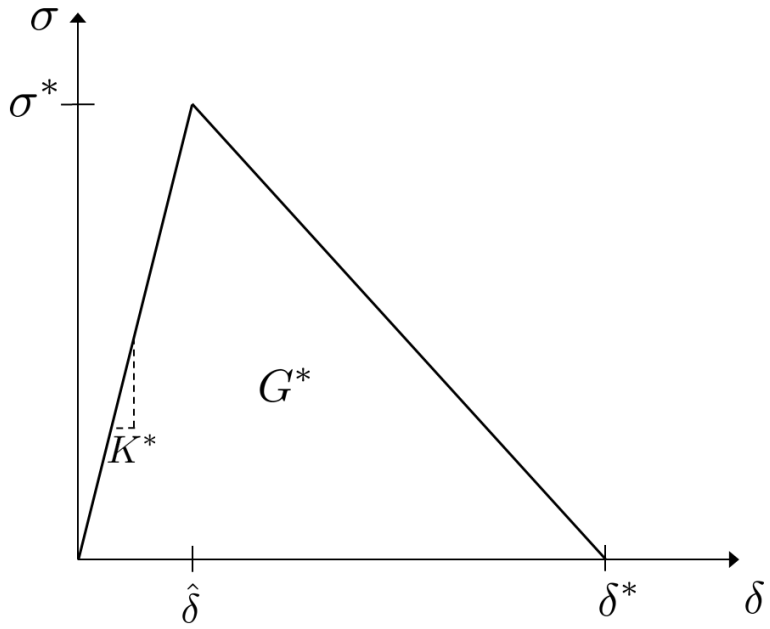

Figure 12: Schematic representation of the traction-separation law and parameters involved.

cohesive zone model [43–47] that can be mathematically expressed as follows

$$\sigma = \begin{cases} K^* \, \hat{\delta} & \text{if} \quad 0 \leq \delta \leq \hat{\delta} \\ \sigma^* \left(\frac{\delta^* - \delta}{\delta^* - \hat{\delta}} \right) & \text{if} \quad \hat{\delta} \leq \delta \leq \delta^* \\ 0 & \text{if} \quad \delta \geq \delta^* \end{cases} \tag{6}$$

where σ^* is the strength of the bonding interface, $\hat{\delta}$ is the crack opening displacement between surfaces at σ^* and K^* is the interface stiffness. The area below the curve defines the interface fracture energy given by $G^* = \frac{1}{2}\sigma^*\delta^*$. This energy, also referred to as fracture toughness, represents the energy that has been dissipated during the full detachment of the two initially attached surfaces. Regarding the interface stiffness K^*, as it has been checked previously [27], Abaqus calculates automatically the adequate value as a function of the two solid material elements under interaction. This ensures that stiffness of the interface does not alter the global stiffness of the system concrete-glass.

On the other hand, to establish the degree of mesh refinement, this work uses as a reference the critical length given by

$$l_{crit} = \frac{2EG^*}{(\sigma^*)^2}, \tag{7}$$

where E is the Young's modulus of the more compliant material (concrete in this case). This length represents the distance between the interfacial crack tip and the point on the interface where the maximum tensile strength is developed [44, 48]. To obtain accurate results, the element size of the mesh, hereinafter referred to as l_{elem}, has to fulfill the condition $l_{elem} \leq l_{crit}$. This criterion can be obtained from the condition that establishes $\epsilon^* < \epsilon_{coh}$, where $\epsilon^* = \sigma^*/E$ stands for the strain of the interface at the peak value of traction and $\epsilon_{coh} = l_{coh}/l_{elem} = 2G^*/\sigma^*/l_{elem}$ stands for a measure of the maximum cohesive strain allowed by the interface relative to the

surface elements that form it.

3.1.2. Three-dimensional model

According to the definition of the critical element size given by eq.7 and the material properties presented in Table 5, the current model requires an element size that fulfills $l_{elem} < 1$ mm. Taking into account the size of the sample, this condition restricts the level of refinement admissible for 3D calculations because the computational cost becomes unaffordable. In spite of that, simulations with elements with three different sizes, $l_{elem} = 0.5$, 1 and 2.5 mm, have been performed in order to probe into the effect of l_{elem} in the maximum force required to break the glass-concrete interface.

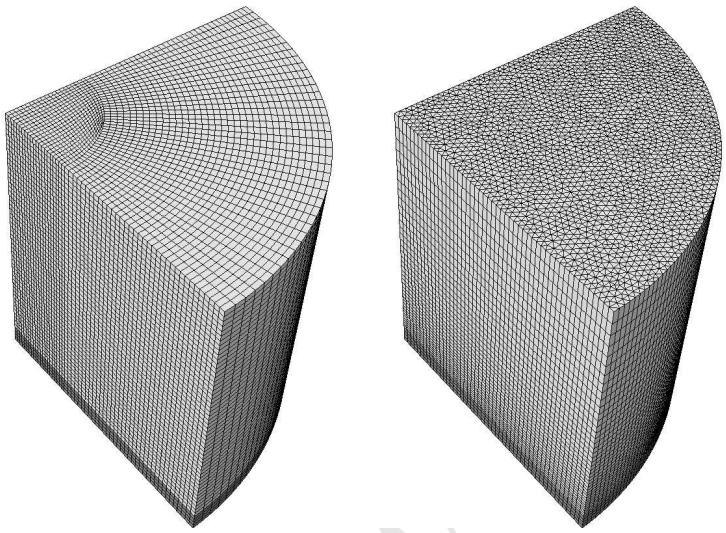

Figure 13: Example of meshes with $l_{elem} = 1$ mm used for 3D models: (left) hexahedral elements and (right) wedge elements.

Figure 13 shows two types of meshes used for this model. The left mesh was created using 8-node hexahedral elements (hereafter denoted by Hex) using linear interpolation and full integration. This type of element corresponds to C3D8 in Abaqus notation [49]. In order to get a regular mesh on the interface plane, an additional partition was performed to obtain concentric layer of elements. As it will be shown later, this regularity exhibits an important difference compared to a non-regular mesh. Additionally, a conformal mesh was chosen to get one-to-one contact elements at the interface between the concrete block and the glass plate. On the other hand, the right mesh in Fig. 13 was created using 6-node wedge elements (hereafter denoted by Wed) with linear interpolation and full integration. In Abaqus notation this element is denoted by C3D6 [49]. The choice of this element type is twofold. Firstly, this element is computationally less expensive than Hex elements (and tetrahedral), although in occasions it requires a finer mesh in regions where the accuracy is critical. This element provides a good compromise between accuracy and performance. Secondly, this element type led to an unstructured triangular mesh along the cross section of the sample, and in particular, on the surfaces where the interface takes place. This mesh geometry makes it possible to avoid any possible preferential direction imposed by the particular geometry of the element (for example, radial and circumferential directions produced by the Hex mesh). Similarly to the previous case, a conformal mesh was also used to mesh the concrete block and the glass plate. The total number of elements generated for the finest meshes ($l_{elem} = 0.5$ mm) was about $8{\cdot}10^5$ elements.

Figure 14 shows the force-displacement curves obtained from the 3D model comparing the usage of Hex and Wed elements as well as different element sizes. Based on the experimental value of the tensile bonding strength introduced in the cohesive interaction and the cross section of the model, a peak force of 7250 N is expected. This value is depicted in Fig. 14 using a thick horizontal line. A first inspection of the global response, using different mesh and element size seems to provide little differences between them. However, all cases have exhibited a peak force slightly lower than the expected value. In fact, looking in more detail into the peak area (zoomed view in Fig. 14), some differences can be appreciated. This result shows that the finest mesh ($l_{elem} = 0.5$ mm) approaches better the expected result, but being still a 3% below. Additionally, using

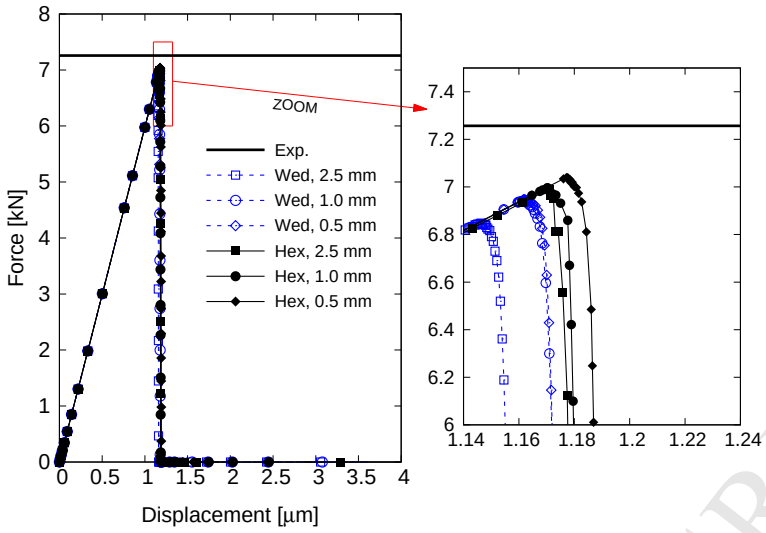

Figure 14: (Left) Force-displacement curves obtained from the 3D tensile test model. Two mesh types are tested: hexahedral (Hex) and wedge (Wed) elements. (Right) Zoomed view around the peak force (same units as the left graph).

Hex elements seems to provide slightly better results than Wed elements. As a matter of fact, the Wed mesh produced the same result for $l_{elem} = 1$ mm and $l_{elem} = 0.5$ mm. This result suggests that the Wed mesh is less sensitive to the element size.

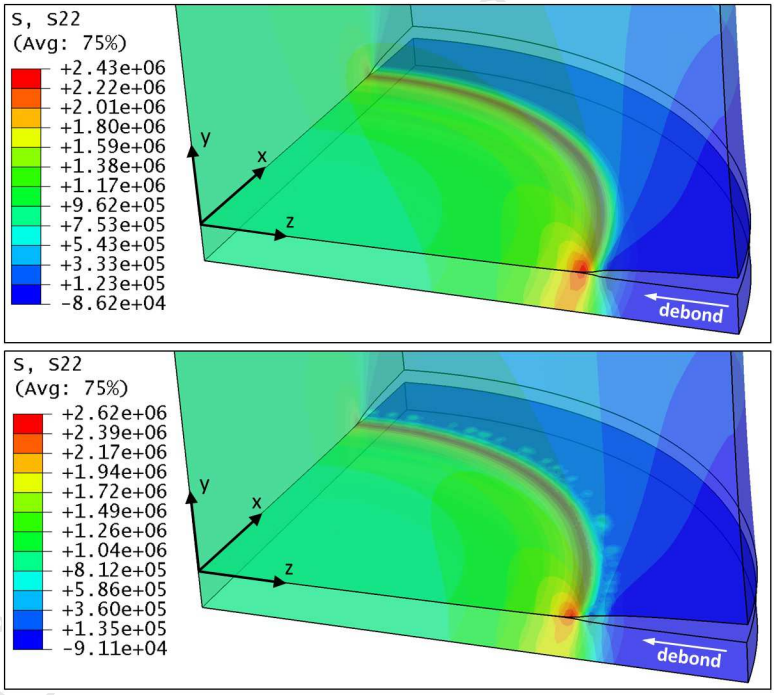

Figure 15: Stress distribution of vertical component (σ_{yy}) plotted on the deformed state during debonding (stress, in Pa, deformation scale factor $\times$ 2000). (Top) Hex mesh. (Bottom) Wed mesh. Element size: $l_{elem} = 0.5$ mm. (For interpretation of the references to color in this figure legend, the reader is referred to the online version of this article).

Regarding the interfacial crack pattern obtained by the model, Fig. 15 shows the aspect of the sample in an intermediate state during debonding. The top image corresponds to Hex mesh and the bottom one to Wed mesh, both with $l_{elem} = 0.5$ mm. For a better visualization, the displacement field has been magnified a factor $\times$ 2000. The stress component perpendicular to the interface (σ_{yy}) is plotted over the sample geometry. The model predicts a concentric-shaped interfacial debonding that is initiated in the most external circular line that joins both material surfaces. This circular crack front advances homogeneously until reaching the center of the sample. Although both meshes have produced similar patterns, the mesh created with Wed elements exhibits a slightly more erratic stress profile in the area behind the crack front. This lack of homogeneity might be

attributed to a less accurate description obtained by using Wed elements [49].

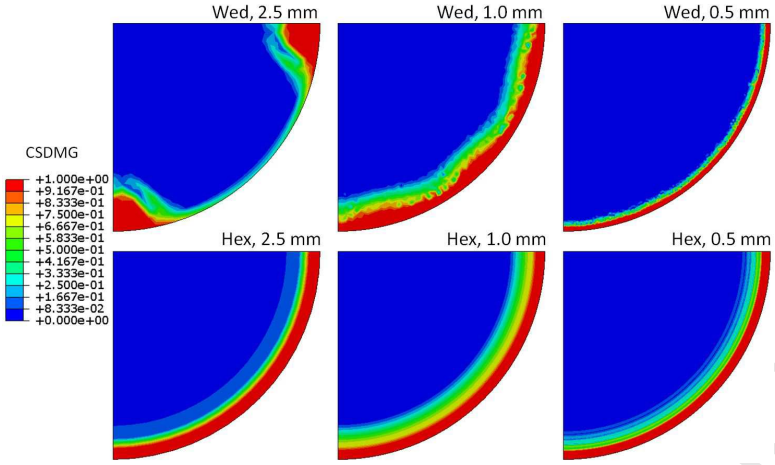

Figure 16: Pattern of interfacial failure provided by the cohesive damage variable CSDMG (0=undamaged, 1=fully damaged). Hex and Wed meshes are compared using different refinement levels. (For interpretation of the references to color in this figure legend, the reader is referred to the online version of this article).

Figure 16 shows the cohesive damage variable associated to the glass-concrete interface. Hex and Wed meshes and the three element sizes are compared at the beginning of the debonding process. CSDMG is a continuous variable whose values are within the interval [0,1]. A value equal to 0 indicates a fully intact interface. A situation with $0 <$ CSDMG < 1 indicates a certain level of damage, although the interface can still carry stresses. If CSDMG equals 1, the interface is fully damaged and stresses cannot be transferred anymore. The results show an important effect of the element size when using a Wed mesh. This type of mesh has to be refined below the size established by the l_{crit} in order to obtain accurate results. For inadequate element length, the debonding initiation is triggered first on the two ends of the contact line and a non-concentric debonding pattern is produced. Interestingly, despite this apparently strong mesh dependence, the total force calculated at debonding only deviates 5.5% with respect to the expected value (see Fig. 14). On the other hand, the model using a Hex mesh has exhibited less mesh dependence regarding the geometry of initiation and propagation of the interface crack. This result suggests that its particular geometry (with circumferential and radial alignment of elements) has had a beneficial effect even for coarse elements. This has not been the case for an unstructured mesh, where the level of refinement has to be bigger.

Nevertheless, the smallest element size used in this 3D model could be considered yet not sufficiently fine, as it is suggested by Turon et al. [50], where a ratio $l_{crit}/l_{elem} \geq 3$ is recommended to get accurate results. Since the computational cost involved in further mesh refinement becomes prohibitive in this 3D model, a deeper analysis for the axisymmetric model has been performed. However, it is worth mentioning that even using a still relatively large element size for this 3D model, their predictions produce quite reliable values in comparison to its more refined axisymmetric counterpart model (see next section).

3.1.3. Axisymmetric model

This section addresses the previous configuration assuming axisymmetric conditions. As before, two types of mesh have been studied: one mesh, denoted by Qua, constructed using 4-node bilinear axisymmetric quadrilateral elements (CAX4), and another mesh, denoted by Tri, created using 3-node linear axisymmetric triangle elements (CAX3). The calculations done in all cases were performed using linear interpolation and full integration. The axisymmetric approach makes it possible to work with much finer meshes, and therefore, for each mesh type, five element sizes have been studied: $l_{elem} = 2$, 1, 0.5, 0.25 and 0.1 mm. As example, Fig. 17 shows the differences between a Qua mesh (left) and a Tri mesh (right), where both cases correspond to $l_{elem} = 1$ mm. Again, regarding the glass-concrete interface, all meshes studied in this section have been set conformal. In this case, the number of elements generated for the finest meshes (0.1 mm) was about $3{\cdot}10^5$ elements.

Figure 18 shows the force-displacement response from the axisymmetric model. Curves in black color correspond to results obtained using a Qua mesh, whereas curves in blue color correspond to a Tri mesh. Similarly to the previous case, the experimental force value required to debond both parts of the sample has

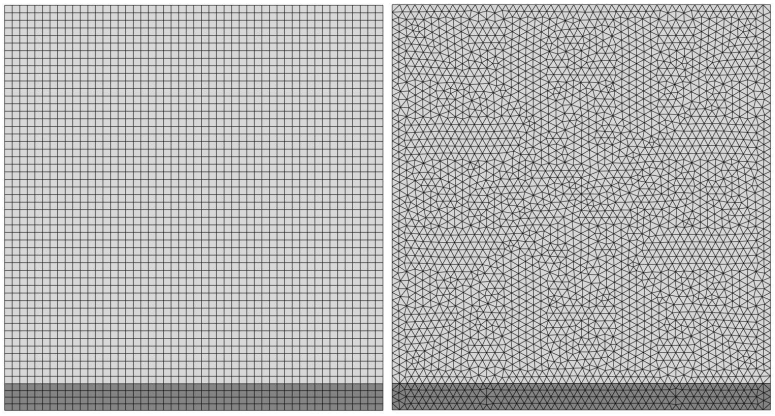

Figure 17: Example of mesh with $l_{elem} = 1$ mm used for Axi models: Quadrilateral elements (left) and Triangular elements (right).

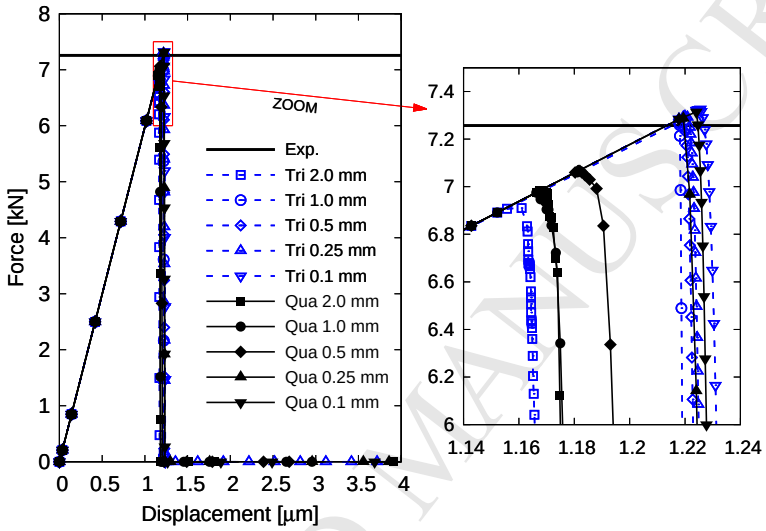

Figure 18: (Left) Force-displacement curves obtained from the Axisymmetric tensile test model. Two mesh types are tested: quadrilateral (Qua) and triangular (Tri) elements. (Right) Zoomed view around the peak force (same units as the left graph).

been indicated using a thick horizontal line. Also, on the right side of this figure, a zoomed view bounding the area around the peak force has been plotted. In order to facilitate the comparison with the 3D model, this figure and its zoomed view use the same scale as in Fig. 14. Results obtained from using a Qua mesh reveal a very similar behavior to the 3D model. As it can be seen in the zoomed view of Fig. 18, using element sizes of 1 mm and 2 mm produced essentially the same response, similarly to what happened in the 3D model when sizes of 1 mm and 2.5 mm were used. Additionally, for $l_{elem} = 0.5$ mm the axisymmetric and 3D model have produced very similar peak forces, 7060 N and 7040 N, respectively. In this occasion, a finer refinement of the mesh has made it possible to reach the experimental value, as expected for $l_{crit}/l_{elem} > 3$. This convergence to the experimental value has been reached even sooner using a Tri mesh, particularly for $l_{elem} \approx l_{crit}$. Moreover, both Qua and Tri geometries meshed with the smallest element size (0.1 mm) have provided a peak force 0.8% larger than the experimental value.

The distribution of the normal interfacial force between glass and concrete is presented in Fig. 19. The top image shows this distribution when the total load undergone by the sample has reached the peak value that triggers the debonding (see Fig.18). As it can be seen, the interface force exhibits a clear linear distribution along the radial coordinate. A fast estimation to check whether this profile matches properly the total peak force can be performed as follows. The element size used in this example is $l_{elem} = 0.5$ mm, which amounts to a total of $n = 101$ nodes along the radius of the sample. The resulting linear distribution makes it possible to write the force directly on the i-*th* node as $F_i \approx F_{max}\, i/n$, where $F_{max} \approx 139$ N is the maximum value of the distribution shown in the scale. Also, it can be assumed that node $i = 0$ is located in the center of the sample and node $i = 100$ is the last node located at the edge of the interface. Therefore, performing the sum over all

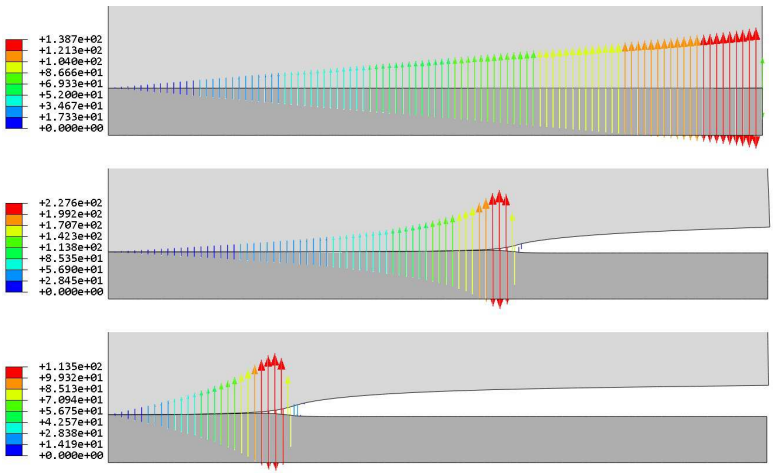

Figure 19: Example of distribution of normal force along the interfacial crack (Qua mesh, $l_{elem} = 0.5$ mm, force in N, displacement scale factor × 2000). Three stages are shown: (top) beginning of debonding at the peak force, (center) intermediate state and (bottom) state almost before total interfacial failure. (For interpretation of the references to color in this figure legend, the reader is referred to the online version of this article).

nodes in the interface, the total force obtained is $F = F_{max}(n+1)/2 \approx 7090$ N, whose value matches perfectly the total peak force to initiate the debonding for this case (see zoomed view of Fig. 18). Once the interface crack starts to propagate, the force distribution changes to a nonlinear function according to the acquired shape of the crack opening [51, 52], as it is shown in the central and bottom images of Fig. 19.

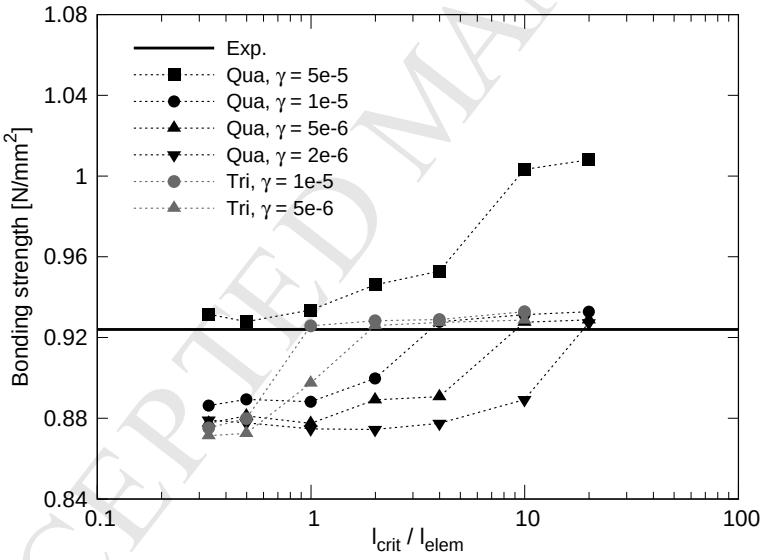

Figure 20: Bonding strength values obtained from the axi-symmetrical model. Convergence analysis: element size, numerical damping and type of mesh.

Implicit solvers dealing with discontinuities, softening processes or material degradation typically make use of a viscous regularization to overcome convergence difficulties. Specific or advisable values of this regularization are not usually found in the literature where numerical models are applied to engineering problems. Abaqus solver is endowed with a built-in regularization scheme to reach convergence while having a minimal effect on the response. The amount of regularization is governed by the parameter denoted here by γ and it makes the consistent tangent stiffness of the softening interaction law positive for sufficiently small time increments [49]. The amount of viscous regularization established by default in Abaqus is $\gamma = 10^{-5}$. Nevertheless, this value might change for specific problems and therefore it demands a preliminary analysis in order to understand and delimit its influence, and consequently, the validity of the final results. This analysis has been carried out for the present axisymmetric model. Results are depicted in Fig. 20. As stated in Abaqus specifications, damage stabilization used to achieve convergence could affect the overall response and, in particular, the post peak region

of the load-displacement curve. Looking at the force-displacement curves of Fig. 18, this stabilization has no visible effects in the post-peak response, mainly due to the high brittleness of the interface, which produces a very fast force drop. However, this stabilization seems to have a non-negligible effect on the peak force itself. This result suggests that the value of γ has to be chosen carefully, and not only as a function of the ratio l_{crit}/l_{elem}, but also considering the element type.

3.2. Simulation of the four point bending test setup

According to the analysis obtained from the previous models and taking into account the extreme brittle nature of the glass-concrete interface, the present model has been built up using the Virtual Crack Closure Technique (VCCT) [53]. As it will be shown in the next section, the approach of this formulation is energy-based and does not require the usage of the maximum bonding tensile strength σ^*. With this situation it is possible to evade the restrictions in terms of mesh size established by eq. 7 due to the dimensions involved in the sample size. Similarly, the usage of viscous regularization has not been required, which makes it possible to avoid its influence in the results. However, this approach is not exempted from mesh issues, and therefore a convergence analysis has also been conducted to ensure the validity of the results and further interpretation. On the other hand, due to the geometry, dimensions and symmetry of the problem, a two-dimensional plane strain model has been adopted.

3.2.1. Interface modeling technique

The VCCT approach is based on the principles of the linear elastic fracture mechanics (LEFM) and is more suitable to describe crack propagation in very brittle materials. The concept relies on calculating the strain energy released directly from the calculated forces and displacements at the crack tip. As mentioned before, this is an energy-based technique, therefore the existence of an initial pre-crack is required in order to start the calculation process. As it is shown in Fig. 21, when a crack propagates a small increment distance Δa, the

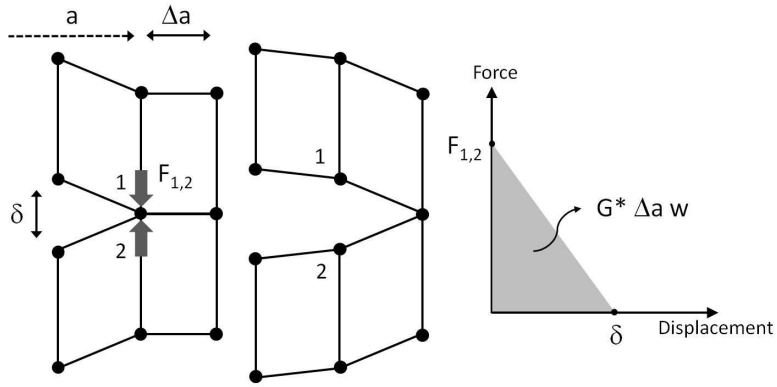

Figure 21: Schematic concept of the Virtual Crack Closure Technique. An interface crack of length a is extended a small amount Δa when the energy released equals the interface toughness G^*. This value of energy would be also required to close the same amount of crack extension.

strain energy released, G^*, is the same as the value of energy needed to close the same distance. Therefore, the interface crack propagates whenever the mechanical condition in the crack tip nodes, denoted by 1 and 2 in Fig. 21, fulfills the following relationship

$$\frac{1}{2} F_{1,2}\, \delta \geq G^*\, \Delta a\, w \tag{8}$$

where $F_{1,2}$ is the force between the nodes at the front, δ is the crack node aperture behind the tip and w is the width of the sample (see Fig. 6). Concerning Mode II, the same argument and equation apply in the tangential direction. This work assumes isotropic interface crack propagation and therefore the same interfacial fracture toughness has been provided for mode I and mode II. As it will be seen, this assumption has provided very good results in comparison with the experimental tests.

3.2.2. Boundary conditions and mesh

Figure 22 shows the schematic representation of the model used to simulate the four point bending setup described in section 2.3.1. This configuration has a symmetry plane located in the middle of the sample length.

This symmetry is imposed by means of restricting the movement in x-direction for nodes of the concrete layer that lie on this plane (dashed line). The lower support of the composite beam is introduced by restricting the movement in y-direction in one point of the glass bottom surface. The composed beam undergoes a displacement-controlled load applied in one point on the top surface of the concrete layer. The procedure to apply this load

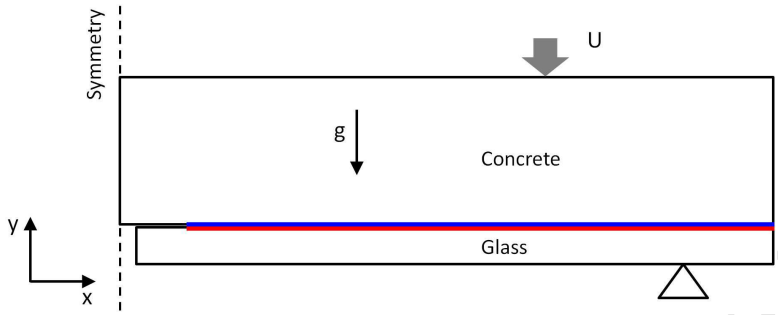

Figure 22: Four point bending model setup: boundary conditions, system of reference, precrack and bonded surfaces affected by the VCCT approach.

is the one described in section 3.1.1, where the maximum imposed displacement was $U = 0.17$ mm. Similarly to the previous tensile test model, this configuration also requires to define two distinct initially bonded contact surfaces between which the crack will propagate: the bottom surface of the concrete block (in blue) and the top surface of the glass plate (in red). However, in this occasion a pre-crack has been included. Both constituents are not connected along this pre-crack, and therefore the nodes that lie on this length are assumed as free faces. Gravity has also been included in the calculation due to the dimension of the glass plate and the level of critical load obtained from the experimental test. Otherwise, neglecting the weight of the plate might overestimate the force required to debond both materials.

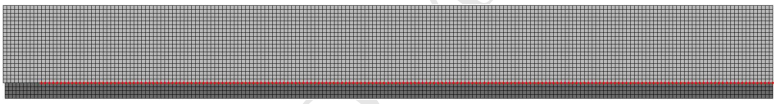

Figure 23: Example of mesh with $l_{elem} = 2$ mm used for the four point bending setup using the VCCT approach.

Figure 23 shows an example of the mesh geometry used for this model using an element size given by $l_{elem} =$ 2 mm. Taking into account the results from the previous model, a 4-node bilinear plane strain quadrilateral (CPE4) mesh element with full integration has been used. This type of element provides a good balance between accuracy and computational effort. On the other hand, with the aim of producing more accurate results, a conformal mesh has been chosen to get one-to-one contact elements at the bonded region between the concrete layer and the glass plate (see red-colored node line in Fig. 23). To analyze the influence of the mesh size in the VCCT approach, five element sizes have been used: l_{elem} =0.5, 1, 2, 3 and 4 mm. The number of elements generated for the coarsest mesh was 1212, whereas the finest mesh produced 76768 elements.

Regarding the materials assigned to every part of the model, the properties presented in Table 5 have been used. As mentioned, this model does not require σ^*. The density of the concrete was 2395 kg/m^3 (see Table 2) and the density of the glass plate was 2500 kg/m^3 [42].

3.2.3. Results

Figure 24 shows the load displacement curves obtained from the four point bending model. Similarly to the experimental results described in section 2.3.3, the simulation model also exhibits the same three-stage behavior: (i) an initial linear bending response before debonding, (ii) a steady-state response where a constant load is obtained and (iii) a second linear response that corresponds to the bending stage undergone only by the concrete part. The steady-state response is depicted in the zoomed view of Fig. 24. In order to check whether crack propagation truly occurs in this narrow interval of beam deflection, five points labeled from (1) to (5) have been indicated. From these states, the profiles of horizontal stresses (σ_{xx}) have been represented in Fig. 25. The mechanical state of point (1) lies in stage (i) where the bending stiffness of the composed beam is active. The stresses are concentrated in the precrack tip but the forces involved along the interface are not

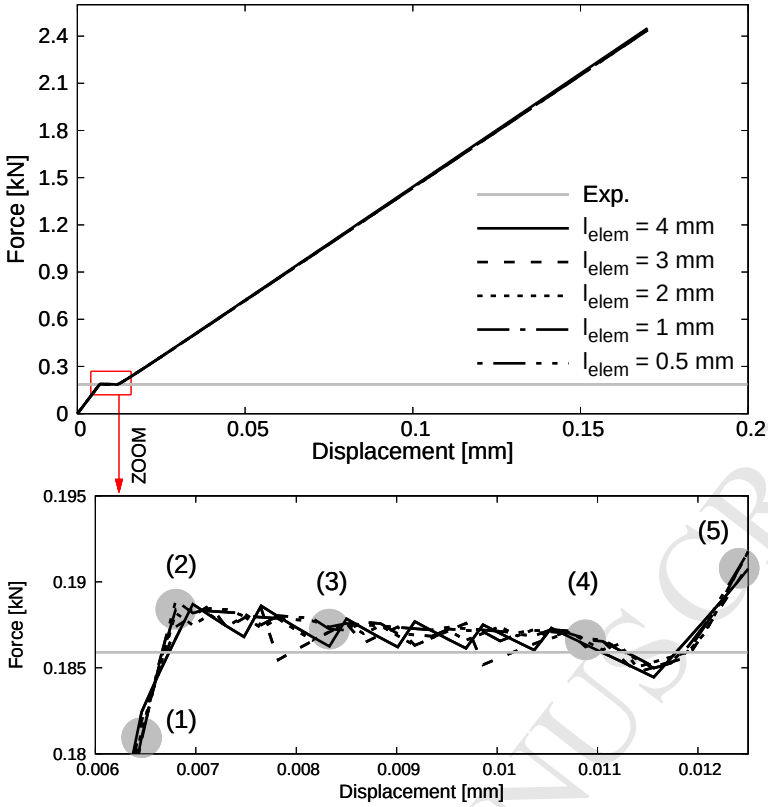

Figure 24: (Top) Force-displacement diagrams obtained from the simulated four point bending model. (Bottom) Zoomed view of the load region corresponding to glass plate debonding.

sufficient to trigger debonding. From point (2) the precrack initiates its propagation and the computed load entered in the regime (ii). The load calculated in points (3) and (4) remains approximately at the same value while the interface crack progresses until covering almost the total distance between the symmetry plane and the loading line. At point (5), the glass plate has reached its maximum level of debonding, and the interfacial crack tip can hardly advance once the location below the load line is reached. Thus, the load starts to increase again and only the concrete part of the beam is resisting the effort of bending. This linear trend continues until reaching the maximum level of imposed displacement. In the real situation, the concrete beam breaks once a load about 2.1 kN is exceeded. In the present numerical model no failure mechanism was accounted for the concrete material and therefore this failure cannot be seen. Nevertheless, the traction stresses in the concrete computed after 2 kN exceed 3 N/mm^2. This value matches closely the maximum tensile strength (3.1 N/mm^2) obtained experimentally for the concrete used in this study (see properties in Table 2).

It is worth mentioning that the displacement range obtained from the simulation is smaller than the experimental one (about a factor of 10). This difference can be explained in terms of the accumulated deformations present in the experimental setup (for example, the strip used at the supports to prevent glass breakage in contact with the steel rollers). Therefore, the recorded displacement is affected by any extra elastic compliance, including the machine's own compliance. Due to this situation, a direct comparison in terms of displacement between the experiment and the model is not possible. A better agreement in terms of displacements could have been obtained if both strips were included at the contact points in the finite element model. In this case, an additional experimental mechanical characterization of this material should have been performed in order to include its Young's modulus, Poisson's ratio and its possible plastic response under higher loads in the model as well. However, as showed in section 2.3, the determination of the interface energy does not require the measurement of the displacement, but only the force (see eq. 3). This situation makes it possible to work with a simpler and more comprehensible model. The computational effort required is also reduced noticeably (the simulations using this model ran in few minutes).

On the other hand, the agreement with the experimental value of load during delamination is very good, where a deviation less than 1% has been obtained. Moreover, this result confirms the suitability of assuming

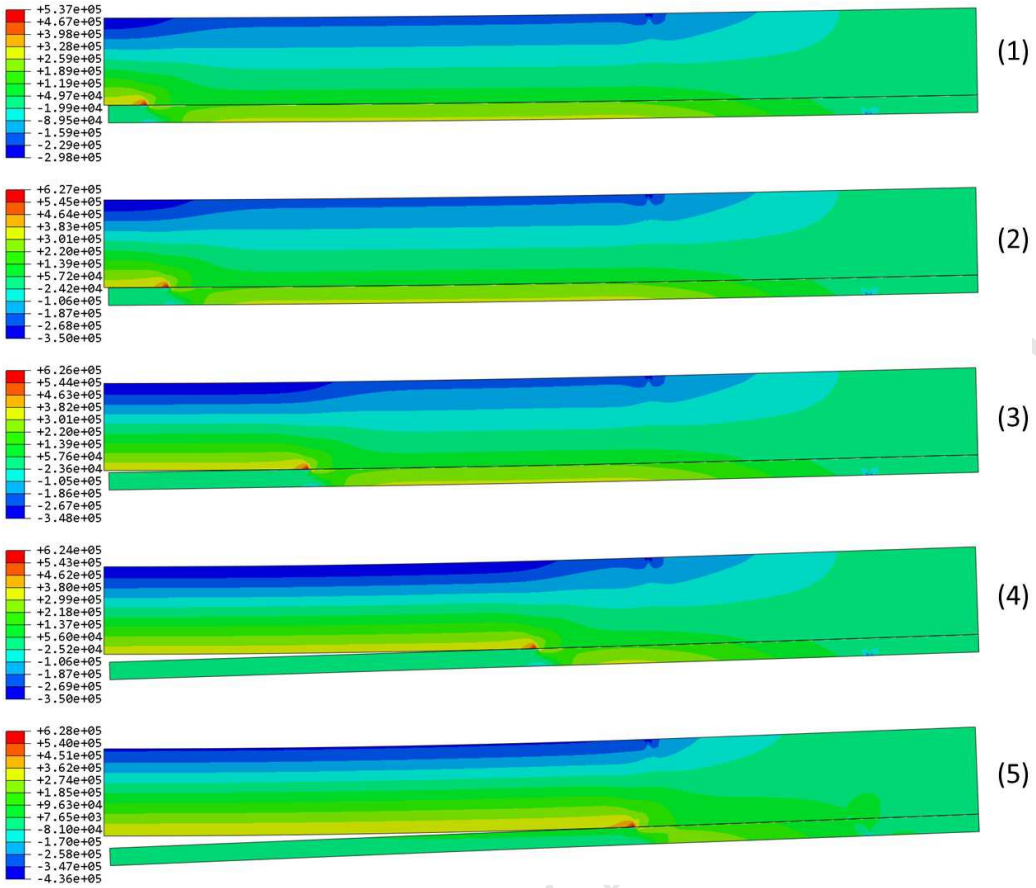

Figure 25: Delamination sequence of the glass plate during the steady-state response in force (see zoomed view of Fig. 24). The profile of horizontal stress σ_{xx} is plotted on the deformed configuration (stress in Pa, displacement scale factor $\times$ 200). See animated version in Fig. 26. (For interpretation of the references to color in this figure legend, the reader is referred to the online version of this article).

isotropy for the propagation mode for this type of brittle interfaces. Regarding the effect of the mesh size, the overlapping between curves from all used element sizes suggests that this simulation model based on the VCCT approach seems to be mesh insensitive.

4. Conclusions

Two experimental setups have been designed to assess the tensile strength and the fracture energy of a glass-concrete interface. This interface is created placing the glass component in contact with fresh concrete, and allowing the bimaterial sample to cure as usually done with pieces only made of concrete. In that sense, additives or special treatment to facilitate or to improve the adherence between both materials have not been used. Every setup required a different design according to the test, however all the produced samples have followed identical procedure and conditions to ensure the same mechanical properties of the concrete and the same interface conditions. A detailed description of the sample designs and preparation processes are provided.

The maximum bonding strength has been obtained with cylindrical-shaped samples subjected to uniaxial tensile loading, where a concrete cylinder is bonded to a thick glass plate. Six samples have been tested and all of them showed a clean debonding between both parts. The average bonding strength obtained was 0.96 ± 0.09 N/mm^2. A companion numerical model has been developed to reproduce and to look more in detail into the debonding process under tensile load. Two different models have been developed (three-dimensional and axisymmetric) using the commercial software Abaqus. Both models are based on the combination of conventional finite element method and cohesive zone model to account for the glass-concrete interface. A rigorous process of numerical validation and mesh effect analysis has been performed with both models. It has been found that the proposed experimental setup can be used to determine directly the maximum tensile strength required by the cohesive zone model. Additionally, the models have provided several insights about the initiation and

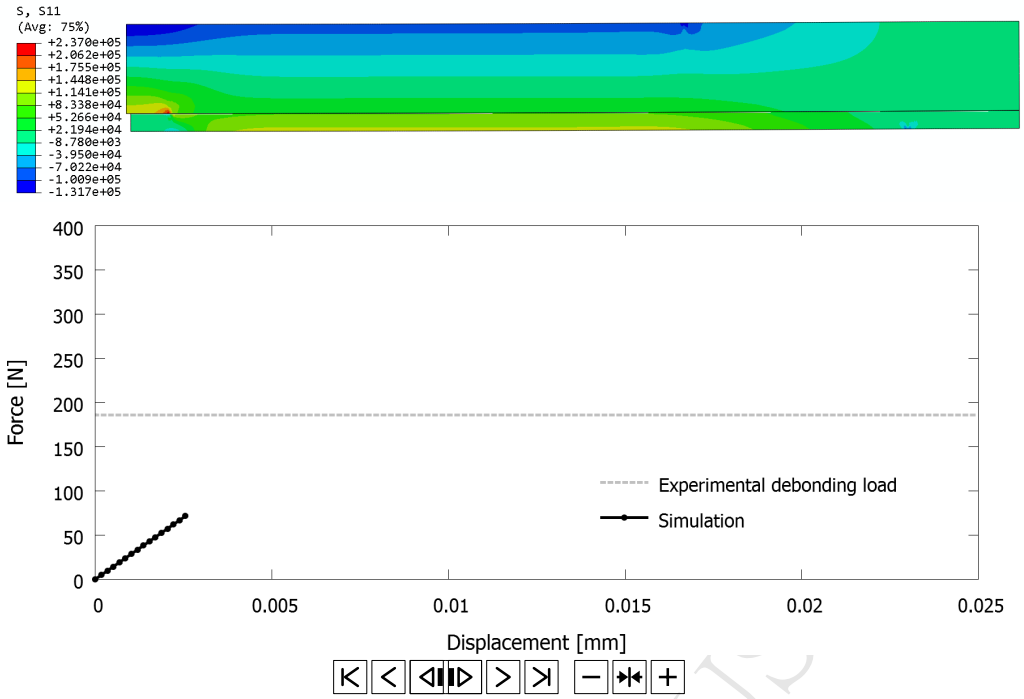

Figure 26: Animation of the delamination process (scale: σ_{xx}, in Pa, displacement scale factor × 200). (For interpretation of the references to color and visualization of the animation, the reader is referred to the online version of this article).

propagation of the interfacial crack as well as the distribution of stresses and forces involved during the process. Numerical recommendations regarding the mesh geometry, element size and viscous regularization are provided.

Regarding the interfacial fracture toughness, the critical energy release rate of the glass-concrete interface has been obtained using a bimaterial beam loaded under four point bending test. The delamination process between both materials is detected due to existence of a steady-state regime in the load-displacement curve. The load recorded during this stationary regime, together with the beam geometry and its elastic properties have been related to the interface energy release rate via an analytical equation. Four bimaterial beams have been tested, and all of them have generated the same mechanical response. The results have revealed a very brittle response of glass debonding, which occurs in a very narrow range of deflection of the beam. The average interface fracture energy obtained was 10.62 ± 0.02 mJ/m^2. This brittle behavior has been reproduced and verified via a companion numerical model. This model has also been developed using the finite element method, however, in this occasion, the glass-concrete interface has been implemented using the virtual crack closure technique. This technique is an energy-based approach that makes it possible to avoid some numerical drawbacks existing in the cohesive zone model approach. Similarly to the tensile test, a mesh convergence analysis has also been performed to guarantee the reliability of the results. Due to the load condition, symmetry of the geometry and the size of the real sample, a two-dimensional plain strain model has been adopted. This model has shown an excellent agreement with the experimental results, confirming the experimental observation about how and when the initial interface precrack propagates until the total failure of the sample.

As a final remark (what has motivated this work) the results of this characterization study, supported via numerical simulations, could be directly used as input data in simulation models dealing with self-healing concrete, and also in any application in civil engineering or architecture, where concrete and glass usually may coexist. Furthermore, the methodology presented in this work, which has proved to provide good results, could also be adapted in principle to characterize other types of bimaterial interface (for example, any possible combinations between ceramics, glass, composites, metals or polymers).

Acknowledgments

Financial support from the Strategic Initiative Materials - Flanders (program Engineered Self-Healing materials (SHE) - project SECEMIN) is gratefully acknowledged. F.A.G. wishes to sincerely thank Mr. Frans

Boulpaep for his assistance to perform the four point bending tests at the MeMC Lab. K.V.T. is a postdoctoral fellow of the Research Foundation - Flanders (FWO, project number 12A3314N) and acknowledges its support.

References

[1] S. R. White, N. R. Sottos, P. H. Geubelle, J. S. Moore, M. R. Kessler, S. R. Sriram, E. N. Brown, S. Viswanathan, Autonomic healing of polymer composites, Nature 409 (2001) 794–7.

[2] S. Van Der Zwaag, A. Schmets, G. Van Der Zaken, Self Healing Materials: An Alternative Approach to 20 Centuries of Materials Science, Springer Series in Materials Science, Springer, 2007.

[3] S. van der Zwaag, N. van Dijk, H. Jonkers, S. Mookhoek, W. Sloof, Self-healing behaviour in man-made engineering materials: bioinspired but taking into account their intrinsic character, Philosophical Transactions of the Royal Society of London A: Mathematical, Physical and Engineering Sciences 367 (2009) 1689–704.

[4] S. Ghosh, Self-healing Materials: Fundamentals, Design Strategies, and Applications, John Wiley & Sons, 2009.

[5] T. D. P. Thao, T. J. S. Johnson, Q. S. Tong, P. S. Dai, Implementation of self-healing in concrete âĂŞ Proof of concept, The IES Journal Part A: Civil & Structural Engineering 2 (2009) 116–25.

[6] K. V. Tittelboom, N. D. Belie, D. V. Loo, P. Jacobs, Self-healing efficiency of cementitious materials containing tubular capsules filled with healing agent, Cement and Concrete Composites 33 (2011) 497–505.

[7] M. Wu, B. Johannesson, M. Geiker, A review: Self-healing in cementitious materials and engineered cementitious composite as a self-healing material, Construction and Building Materials 28 (2012) 571–83.

[8] M. d. Rooij, K. V. Tittelboom, N. D. Belie, E. Schlangen, Self-Healing Phenomena in Cement-Based Materials: State-of-the-Art Report of RILEM Technical Committee 221-SHC: Self-Healing Phenomena in Cement-Based Materials, Springer Science & Business Media, 2013.

[9] K. Van Tittelboom, N. De Belie, Self-healing in cementitious materials - a review, Materials 6 (2013) 2182–217.

[10] A. B. W. Brochu, O. B. Matthys, S. L. Craig, W. M. Reichert, Extended fatigue life of a catalyst free self-healing acrylic bone cement using microencapsulated 2-octyl cyanoacrylate, Journal of Biomedical Materials Research Part B: Applied Biomaterials 103 (2015) 305–12.

[11] M. Kessler, N. Sottos, S. White, Self-healing structural composite materials, Composites Part A: Applied Science and Manufacturing 34 (2003) 743–53.

[12] K. Van Tittelboom, K. Adesanya, D. P., P. Van Puyvelde, N. De Belie, Methyl methacrylate as a healing agent for self-healing cementitious materials, Smart Materials and Structures 20 (2011) 125016/1–12.

[13] Q. G. L. Sun, W. Y. Yu, Experimental research on the self-healing performance of micro-cracks in concrete bridge, Advanced Materials Research 250–253 (2011) 28–32.

[14] M. Maes, K. Van Tittelboom, N. De Belie, The efficiency of self-healing cementitious materials by means of encapsulated polyurethane in chloride containing environments, Construction and Building Materials 71 (2014) 528–37.

[15] E. Tsangouri, G. Karaiskos, D. G. Aggelis, A. Deraemaeker, D. Van Hemelrijck, Crack sealing and damage recovery monitoring of a concrete healing system using embedded piezoelectric transducers, Structural Health Monitoring (2015).

[16] J. Tirosh, A. S. Tetelman, Fracture conditions of a crack approaching a disturbance, International Journal of Fracture 12 (1976) 187–99.

[17] M. G. Knight, L. C. Wrobel, J. L. Henshall, L. A. De Lacerda, A study of the interaction between a propagating crack and an uncoated/coated elastic inclusion using the BE technique, International Journal of Fracture 114 (2002) 47–61.

[18] H. Chandler, I. Merchant, R. Henderson, D. Macphee, Enhanced crack-bridging by unbonded inclusions in a brittle matrix, Journal of the European Ceramic Society 22 (2002) 129–34.

[19] R. Kitey, H. V. Tippur, Dynamic Crack Growth Past a Stiff Inclusion: Optical Investigation of Inclusion Eccentricity and Inclusion-matrix Adhesion Strength, Experimental Mechanics 48 (2008) 37–53.

[20] K. C. Jajam, H. V. Tippur, Role of inclusion stiffness and interfacial strength on dynamic matrix crack growth: An experimental study, International Journal of Solids and Structures 49 (2012) 1127–46.

[21] A. C. Balazs, Modeling self-healing materials, Materials Today 10 (2007) 18–23.

[22] S. V. Zemskov, H. M. Jonkers, F. J. Vermolen, Two analytical models for the probability characteristics of a crack hitting encapsulated particles: Application to self-healing materials, Computational Materials Science 50 (2011) 3323–33.

[23] H. Huang, G. Ye, The effects of capules on self-healing efficiency in cementitious materials, in: Second International Conference on Microstructural-related Durability of Cementitious Composites, RILEM Proceedings pro083, 11-13 April, 2012, Amsterdam, The Netherlands, Rilem, 2012, pp. 1090–100.

[24] Z. Lv, H. Chen, Analytical models for determining the dosage of capsules embedded in self-healing materials, Computational Materials Science 68 (2013) 81–9.

[25] F. A. Gilabert, D. Garoz, W. Van Paepegem, Modelling fracture in micro-encapsulated self-healing materials with combined XFEM and cohesive surface techniques, Technical Report, Regional Benelux ABAQUS User Meeting, Hoeven, Netherlands, 13-14 November, 2013.

[26] H. Huang, G. Ye, Z. Shui, Feasibility of self-healing in cementitious materials - By using capsules or a vascular system?, Construction and Building Materials 63 (2014) 108–18.

[27] F. A. Gilabert, D. Garoz, W. Van Paepegem, Stress concentrations and bonding strength in encapsulation-based self-healing materials, Materials & Design 67 (2015) 28–41.

[28] G. B. Pye, J. J. Beaudoin, An energy approach to bond strength determinations in cement systems, Cement and Concrete Research 22 (1992) 551–8.

[29] J. Zhou, M. Huang, F. Sagnang, W. Soboyejo, Interfacial failure of a dental cement composite bonded to glass substrates, Dental Materials 22 (2006) 585 –91.

[30] K. Van Tittelboom, Self-Healing Concrete through Incorporation of Encapsulated Bacteria- or Polymer-Based Healing Agents, Ph.D. thesis, Ghent University, 2012.

[31] T. D. P. Thao, Quasi-Brittle Self-Healing Materials: Numerical Modelling and Applications in Civil Engineering., Ph.D. thesis, 2011.

[32] X. Wang, F. Xing, M. Zhang, N. Han, Z. Qian, Interaction between microcapsules and cementitious matrix after cracking in a self-healing system, in: ICSHM 2013: Proceedings of the 4th International Conference on Self-Healing Materials, Ghent, Belgium, 16-20 June 2013, Magnel Laboratory for Concrete Research, 2013.

[33] K. Van Tittelboom, J. Wang, M. Araújo, D. Snoeck, E. Gruyaert, B. Debbaut, H. Derluyn, V. Cnudde, E. Tsangouri, D. Van Hemelrijck, N. De Belie, Comparison of different approaches for self-healing concrete in a large-scale lab test, Construction and Building Materials 107 (2016) 125–37.

[34] G. Karaiskos, E. Tsangouri, D. G. Aggelis, K. V. Tittelboom, N. D. Belie, D. V. Hemelrijck, Performance monitoring of large-scale autonomously healed concrete beams under four-point bending through multiple non-destructive testing methods, Smart Materials and Structures 25 (2016) 055003/1–16.

[35] P. G. Charalambides, J. Lund, A. G. Evans, R. M. McMeeking, A Test Specimen for Determining the Fracture Resistance of Bimaterial Interfaces, Journal of Applied Mechanics 56 (1989) 77–82.

[36] P. G. Charalambides, H. C. Cao, J. Lund, A. G. Evans, Development of a test method for measuring the mixed mode fracture resistance of bimaterial interfaces, Mechanics of Materials 8 (1990) 269–83.

[37] P. Tran, S. S. Kandula, P. H. Geubelle, N. R. Sottos, Comparison of dynamic and quasi-static measurements of thin film adhesion, Journal of Physics D: Applied Physics 44 (2011) 034006/1–8.

[38] H. Cao, A. Evans, An experimental study of the fracture resistance of bimaterial interfaces, Mechanics of Materials 7 (1989) 295–304.

[39] I. Hofinger, M. Oechsner, H.-A. Bahr, M. V. Swain, Modified four-point bending specimen for determining the interface fracture energy for thin, brittle layers, International Journal of Fracture 92 (1998) 213–20.

[40] A. Agrawal, A. M. Karlsson, Obtaining mode mixity for a bimaterial interface crack using the virtual crack closure technique, International Journal of Fracture 141 (2006) 75–98.

[41] B. Wang, T. Siegmund, A modified 4-point bend delamination test, Microelectronic Engineering 85 (2008) 477–85.

[42] J. Shackelford, R. Doremus, Ceramic and Glass Materials: Structure, Properties and Processing, Springer, 2010.

[43] G. Barenblatt, The formation of equilibrium cracks during brittle fracture. general ideas and hypotheses. axially-symmetric cracks, Journal of Applied Mathematics and Mechanics 23 (1959) 622–36.

[44] A. Hillerborg, M. Modéer, P.-E. Petersson, Analysis of crack formation and crack growth in concrete by means of fracture mechanics and finite elements, Cement and Concrete Research 6 (1976) 773 –81.

[45] S. H. Song, H. Glaucio, Paulino, G. B. William, A bilinear cohesive zone model tailored for fracture of asphalt concrete considering viscoelastic bulk material, Engineering Fracture Mechanics 73 (2006) 2829–48.

[46] K. Park, G. Paulino, Cohesive zone models: A critical review of traction-separation relationships across fracture surfaces, ASME Applied Mechanics Review 64 (2013) 060802/1–20.

[47] A. Needleman, Some issues in cohesive surface modeling, Procedia {IUTAM} 10 (2014) 221–46. Mechanics for the World: Proceedings of the 23rd International Congress of Theoretical and Applied Mechanics, {ICTAM2012}.

[48] G. Barenblatt, The mathematical theory of equilibrium cracks in brittle fracture, volume 7 of *Advances in Applied Mechanics*, Elsevier, 1962, pp. 55–129.

[49] ABAQUS 6.14 User Documentation, Technical Report, Dassault Systémes Simulia Corp., Providence, RI, USA., 2014.

[50] A. Turon, C. Dávila, P. Camanho, J. Costa, An engineering solution for mesh size effects in the simulation of delamination using cohesive zone models, Engineering Fracture Mechanics 74 (2007) 1665–82.

[51] E. E. Gdoutos, Fracture Mechanics. An Introduction, Springer Netherlands, 2005.

[52] T. L. Anderson, Fracture Mechanics. Fundamentals and Applications, Francis & Taylor, Boca Raton, Florida, 2005.

[53] R. Krueger, The virtual crack closure technique, Technical Report CR-2002-211628, NASA, 2000.